

# **SANDIA REPORT**

SAND2017-8965

Unlimited Release

Printed August 2017

# **Microstructural Modeling of Brittle Materials for Enhanced Performance and Reliability**

Melissa C. Teague, Theron Rodgers, Scott Grutzik, Stephen Meserole

Prepared by

Sandia National Laboratories

Albuquerque, New Mexico 87185 and Livermore, California 94550

Sandia National Laboratories is a multimission laboratory managed and operated by National Technology and Engineering Solutions of Sandia, LLC, a wholly owned subsidiary of Honeywell International, Inc., for the U.S. Department of Energy's National Nuclear Security Administration under contract DE-NA0003525.



**Sandia National Laboratories**

Issued by Sandia National Laboratories, operated for the United States Department of Energy by National Technology and Engineering Solutions of Sandia, LLC.

**NOTICE:** This report was prepared as an account of work sponsored by an agency of the United States Government. Neither the United States Government, nor any agency thereof, nor any of their employees, nor any of their contractors, subcontractors, or their employees, make any warranty, express or implied, or assume any legal liability or responsibility for the accuracy, completeness, or usefulness of any information, apparatus, product, or process disclosed, or represent that its use would not infringe privately owned rights. Reference herein to any specific commercial product, process, or service by trade name, trademark, manufacturer, or otherwise, does not necessarily constitute or imply its endorsement, recommendation, or favoring by the United States Government, any agency thereof, or any of their contractors or subcontractors. The views and opinions expressed herein do not necessarily state or reflect those of the United States Government, any agency thereof, or any of their contractors.

Printed in the United States of America. This report has been reproduced directly from the best available copy.

Available to DOE and DOE contractors from

U.S. Department of Energy  
Office of Scientific and Technical Information  
P.O. Box 62  
Oak Ridge, TN 37831

Telephone: (865) 576-8401  
Facsimile: (865) 576-5728  
E-Mail: [reports@osti.gov](mailto:reports@osti.gov)  
Online ordering: <http://www.osti.gov/scitech>

Available to the public from

U.S. Department of Commerce  
National Technical Information Service  
5301 Shawnee Rd  
Alexandria, VA 22312

Telephone: (800) 553-6847  
Facsimile: (703) 605-6900  
E-Mail: [orders@ntis.gov](mailto:orders@ntis.gov)  
Online order: <http://www.ntis.gov/search>



## **Microstructural Modeling of Brittle Materials for Enhanced Performance and Reliability**

Melissa C. Teague<sup>1</sup> Theron Rodgers<sup>2</sup>, Scott Grutzik<sup>3</sup>, Stephen Meserole<sup>4</sup>

1. Vulnerability Capability Unit  
Sandia National Laboratories  
P. O. Box 5800  
Albuquerque, New Mexico 87185-MS0549

2. Computational Materials and Data Science  
Sandia National Laboratories  
P. O. Box 5800  
Albuquerque, New Mexico 87185-MS1411

3. Component Science and Mechanics  
Sandia National Laboratories  
P. O. Box 5800  
Albuquerque, New Mexico 87185-MS0346

4. Electronic, Optical, and Nano  
Sandia National Laboratories  
P. O. Box 5800  
Albuquerque, New Mexico 87185-MS1411

## **Abstract**

Brittle failure is often influenced by difficult to measure and variable microstructure-scale stresses. Recent advances in photoluminescence spectroscopy (PLS), including improved confocal laser measurement and rapid spectroscopic data collection have established the potential to map stresses with microscale spatial resolution (<2 microns). Advanced PLS was successfully used to investigate both residual and externally applied stresses in polycrystalline alumina at the microstructure scale. The measured average stresses matched those estimated from beam theory to within one standard deviation, validating the technique. Modeling the residual stresses within the microstructure produced general agreement in comparison with the

experimentally measured results. Microstructure scale modeling is primed to take advantage of advanced PLS to enable its refinement and validation, eventually enabling microstructure modeling to become a predictive tool for brittle materials.

## TABLE OF CONTENTS

1.	Introduction.....	7
2.	Experimental procedure .....	7
2.1.	Materials [Heading 2] .....	7
2.2.	Electron Backscatter diffraction (EBSD).....	7
2.3.	Photoluminescence Measurements .....	8
2.4.	Analysis of Photoluminescence data .....	9
3.	Modeling Methods and Background.....	10
4.	Results and Discussion .....	11
4.1.	Experimental .....	11
4.2.	Modeling .....	14
5.	Conclusions.....	16
6.	Acknowledgements.....	16
	References 18	

## FIGURES

Figure 1: Representative PLS spectrum with R1, R2, and Ar reference line labeled. ....	8
Figure 2: a) Inverse pole figure of alumina used for mesh generation b) mesh generated using OOF2 from microstructure. ....	11
Figure 3: Inverse pole figure (a) and R1 intensity map (b), showing the inability of intensity maps to detect adjacent grains with similar orientations (grain 1 and 2). ....	13
Figure 4: $\sigma_m$ PLS maps of region with a) zero applied $\sigma_m$ b) 33.3 MPa applied $\sigma_m$ c) 50 MPa applied $\sigma_m$ .....	13
Figure 5: Stress distribution of three loading conditions.....	14
Figure 6: Simulated $\sigma_m$ maps for three loading conditions a) zero applied $\sigma_m$ b) 33.3 MPa applied $\sigma_m$ c) 50 MPa applied $\sigma_m$ .....	15

## TABLES

Table 1: Material Coefficients used for Peak Shift Conversions[13] .....	9
Table 2: Measured stresses as function of applied load.....	14
Table 3: Calculated stresses as function of applied load and averaging area. ....	16

## NOMENCLATURE

Abbreviation	Definition
<b>EBSD</b>	Electron backscatter diffraction
<b>FE</b>	Finite element
<b>IPF</b>	Inverse pole figure
<b>PLS</b>	Photoluminescence spectroscopy

## 1. INTRODUCTION

Understanding failure in brittle materials is critical to predicting and ensuring brittle material performance and long-term reliability in service [1]. To mitigate the risk of catastrophic failure, the current practice is to employ engineering judgment supported by continuum-scale finite element (FE) modeling to ensure maximum stresses remain below the critical failure stress [2]. Unfortunately, the conservative safety factors employed to compensate for the unquantifiable uncertainty in legacy continuum FE model stress predictions is becoming more and more impractical when complex assemblies push brittle materials to their limits. Higher fidelity stress modeling is required to lower uncertainty and design margins[3]. Recognizing that brittle materials fail well below their theoretical bond strength because of microstructure-scale defects, it is critical to predict stress with higher fidelity on the micro-scale. Additionally, models must include the capability to predict the stress intensification associated with continuum stress field interactions with micro-scale defects [4].

Previous modeling efforts focused on idealized analytical methods for prototypic microstructure features such as grain size, shape, and porosity. Some recent efforts utilize actual microstructures to model and predict the effect of real microstructure features on residual and applied stresses [5-10]. These modeling efforts have been hampered by a lack of experimental methods to validate the behavior at the microstructure level. Existing experimental methods include bulk and spatially resolved stress measurements down to the 50-100 micron level using micro-XRD, neutron diffraction and Raman/fluorescence spectroscopy [6, 7, 11]. Recent advances in photoluminescence spectroscopy (PLS) have enabled the measurement of stress at the microstructural scale. Photoluminescence spectroscopy has been found to achieve stress resolution of +/- 1 MPa at spatial resolution of ~0.6 microns[12, 13].

This work expands on the previously reported work by measuring not only residual stresses from manufacturing but also studies the effect of external loading on the microstructure-scale stresses in polycrystalline alumina. The experimental results were compared with a microstructure-scale model of stress behavior, which incorporated the experimental microstructure as measured using electron backscatter diffraction (EBSD).

## 2. EXPERIMENTAL PROCEDURE

### 2.1. Materials

PLS and EBSD measurements were performed on a polished Cr doped alumina sample. Detailed analysis of microstructure and the fabrication process was discussed previously[14]. In brief, the sample began as 99.5% pure alumina that was infiltrated with Cr solution and sintered at 1600°C in H<sub>2</sub> for 18 hrs. Nominal grain size was found to be 20µm, with some grains as large as 60 µm observed. Previous microprobe analysis found the process resulted in a Cr content of 0.025 wt.% [14].

## 2.2. Electron Backscatter diffraction (EBSD)

EBSD was performed on the polycrystalline sample to obtain correlated orientations of each grain for use in modeling. The EBSD result was collected on a Zeiss Supra 55vp (Zeiss, Oberkochen, Germany) with a Bruker Quantax CrystAlign EBSD detector (Bruker, Billerica, MA, USA). An accelerating voltage of 20 KeV and step size of 0.79  $\mu\text{m}$  was used for collection. Post-processing of the EBSD data analysis was performed using EDAX OIM 8.0 (EDAX, Mahwah, NJ, USA).

## 2.3. Photoluminescence Measurements

Photoluminescence spectroscopy was used to measure the position and relative change of the R1 and R2 Cr emission peaks, which as described later (Section 2.4) were then converted to stress values. A representative spectrum is shown in *Figure 1*. All measurements were performed using a LabRamHR (Horiba, Kyoto, JP). A Quantus MPC6000 532 nm laser (Quantum Laser, Manchester, England) was used for all luminescence measurements. The signal was collected using a 2400  $\text{mm}^{-1}$  grating over the 14340-14480  $\text{cm}^{-1}$  range resulting in a pixel resolution of 0.058  $\text{cm}^{-1}$  /pixel. An argon lamp (Pen-Ray #6030, UVP, Upland, CA) was used to generate a reference argon line at 14356.61  $\text{cm}^{-1}$ , which was measured for all collected spectrum to account for optical drift of the instrument. To account for thermal shifting effects, a thermocouple was installed on the sample stage and temperature measurements were recorded during all measurements. LabSpec 6 (Horiba, Kyoto, JP) software was used for both data acquisition as well as peak fitting analysis. The peak center positions were fitted using Gaussian-Lorentzian shape factor.

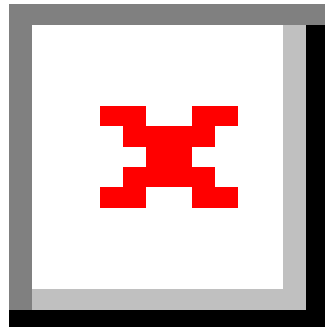


*Figure 1: Representative PLS spectrum with R1, R2, and Ar reference line labeled.*

Stress-free reference positions for alumina using single point spectrums were collected on a m-plane sapphire single crystal (MTI Corp Richmond, CA). A total of 45 spectra

were collected and then averaged to set the stress-free, assumed Cr free position for R1 and R2 spectra lines. A 50x objective was used resulting in a laser spot size of  $\sim 0.87 \mu\text{m}$ . A dwell time of 15 seconds was used for collection. The measured peak positions, adjusted to 298.8 K, were  $\text{R1}=14402.209\pm.02 \text{ cm}^{-1}$  and  $\text{R2}=14432.218\pm.01 \text{ cm}^{-1}$ , which are within range of the previously reported values [15].

Polycrystalline measurements were performed by mapping a 256 by 202  $\mu\text{m}$  rectangle encompassing gold fiducial lines for alignment with EBSD maps, using a  $2 \mu\text{m}$  step size. A 50x objective was used resulting a laser spot size of  $\sim 0.87 \mu\text{m}$ . A dwell time used for collection was decreased to 3 seconds due to the higher Cr concentration, and total of 5 spectrums per step were collected and averaged. The same area was then scanned while a load was applied. A tensile stage (Microtest Vertile Bending 2kN, Deben, London, UK) with a four-point bend fixture was used to apply uniaxial stress states of 0, 100, and 150 MPa to the sample.

## 2.4. Analysis of Photoluminescence data

The methodology for converting the peak positions measured in PLS to stress is discussed in this section. Both R1 and R2 positions are affected by stress, temperature, and chrome composition as seen in equation 1.

$$v^{(i)} = v_0^{(i)} + \Delta v_s^{(i)} + \Delta v_T^{(i)} + \Delta v_C^{(i)} \quad (1a)$$

$$= v_0^{(i)} + \Pi_{jk}^{(i)} \sigma_{jk} + (1) \alpha_T^{(i)} (T - 298.8) + \beta^{(i)} C_m \quad (1b)$$

where  $i$  is 1 or 2 referring to the R1 and R2 peaks respectively  $v$  is peak position,  $v_0^{(i)}$  is reference stress free peak position at 298.8K and negligible Cr composition,  $\Delta v_s$  is peak shift due to stress,  $\Delta v_T$  is shift due to temperature,  $\Delta v_C$  is shift due to Cr composition,  $T$  is temperature in K,  $C_m$  is Cr concentration in mass fraction, and  $\sigma_{jk}$  is stress[13].  $\Pi_{jk}^{(i)}$ ,  $\alpha_T^{(i)}$ , and  $\beta^{(i)}$  are material dependent coefficients and are given in *Table 1* for alumina. The crystal symmetry of alumina provides that only the diagonal elements of  $\Pi_{jk}^{(i)}$  are non-zero and that  $\Pi_{11}^{(i)} = \Pi_{22}^{(i)}$ .

*Table 1: Material Coefficients used for Peak Shift Conversions[13]*

Coefficient	R1	R2
$\alpha_T$	$-0.130 \text{ cm}^{-1}/\text{K}$	$-0.122 \text{ cm}^{-1}/\text{K}$
$\beta$	$160 \text{ cm}^{-1}$	$167 \text{ cm}^{-1}$
$\Pi_{11}$	$3.03 \text{ cm}^{-1}/\text{GPa}$	$1.53 \text{ cm}^{-1}/\text{GPa}$
$\Pi_{33}$	$2.73 \text{ cm}^{-1}/\text{GPa}$	$2.16 \text{ cm}^{-1}/\text{GPa}$

Historically work was focused on making mesoscale measurements that sample many grains at a time [16, 17], in these cases an isotropy argument assuming random crystal orientations and the peak shifts due to stress reduces to

$$\Delta v^{(i)} = \Pi_M^{(i)} \sigma_M \quad (2)$$

Where  $\Pi_M^{(i)} = (2\Pi_{11} + \Pi_{33})$  and  $\sigma_M = 1/3(\sigma_{11} + \sigma_{22} + \sigma_{33})$  Equation (2) relates a mean stress to a single peak shift, therefore either R1 or R2 can be used.

Recently researchers have expanded on this approach by mapping at sub-granular length scales, such as in this work[12, 13]. The assumption of isotropy no longer holds within a single crystal; however, due to the approximately hexagonal symmetry of  $\text{Al}_2\text{O}_3$  peak shifts due to stress can be expressed as

$$\begin{bmatrix} \Delta v^{(1)} \\ \Delta v^{(2)} \end{bmatrix} = \begin{bmatrix} \Pi_M^{(1)} & \Pi_S^{(1)} \\ \Pi_M^{(2)} & \Pi_S^{(2)} \end{bmatrix} \begin{bmatrix} \sigma_M \\ \sigma_S \end{bmatrix} \quad (3)$$

where  $\Pi_M^{(i)} = (2\Pi_{11} + \Pi_{33})$ ,  $\Pi_s = (\Pi_{33} - \Pi_{11})$ ,  $\sigma_s = 2\sigma_{33} - \sigma_{11} - \sigma_{22}/3$ ,  $\sigma_M = (\sigma_{11} + \sigma_{22} + \sigma_{33})/3$ . By measuring R1 and R2 peak shifts the stresses  $\sigma_M$  and  $\sigma_s$  can be found by inverting equation (3)[13, 15].

### 3. MODELING METHODS AND BACKGROUND

#### Microstructure Meshing

Microstructure modeling was performed to simulate the experiments conducted. To allow direct comparison between experiments and modeling the experimental microstructures were imported for use in modeling efforts. Finite element meshes were generated by importing the EBSD data into OOF2 (NIST, Gaithersburg, MA)[18]. A comparison between the source EBSD data and the resulting finite element mesh is shown in Figure 2.

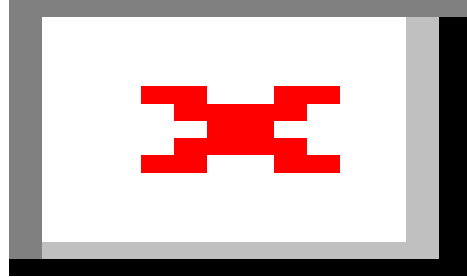


Figure 2: a) Inverse pole figure of alumina used for mesh generation b) mesh generated using OOF2 from microstructure.

### Stress Modeling

The OOF2-generated meshes were used to perform stress modeling using the Tensor Mechanics physics module of the MOOSE finite element package (Idaho National Laboratory, Idaho Falls, ID)[19]. In addition to grain morphologies, the EBSD scans also provided orientations for each grain in the microstructure, enabling modeling of the anisotropic properties in alumina. The elastic constants for corundum alumina used for the analysis were:  $c_{11}=497.3$  GPa  $c_{33}=500.9$  GPa  $c_{44}=146.8$ ,  $c_{12}=162.8$ ,  $c_{13}=116.0$  Gpa,  $c_{14}=-21.9$  GPa [20]. The average thermal expansion over the temperature range was used, for the analysis  $\alpha_{11}$  was taken as  $7.29 \times 10^{-6}/^\circ\text{C}$  and  $\alpha_{33}$  as  $8.19 \times 10^{-6}/^\circ\text{C}$ [21].

An initial condition 1600°C was applied to the model to create a stress-free state at the sintering temperature. The model was then cooled to 27°C inducing a residual stress due to the anisotropic thermal expansions of the grains. These conditions assume that the grain boundaries are locked and that stress begins to accumulate immediately upon cooling. The residual stress models were run assuming a 2D microstructure and using plane stress (assuming  $\sigma_{33}$  is zero), with no constraints applied to the boundaries. The applied stress models were also run with assumed plane stress, with constant pressure applied to the left and right boundaries (corresponding to the experimentally applied stresses), while, the top and bottom boundaries were left unconstrained to simulate uniaxial stress state of the 4pt bend test.

## 4. RESULTS AND DISCUSSION

### 4.1. Experimental

The R1 peak intensity map from polycrystalline sample along with an inverse pole figure (IPF) obtained from EBSD are shown in *Figure 3*. Previous studies have used

intensity maps to determine microstructure due to the varying intensity as function of grain orientation [12, 13]. However, as seen in *Figure 3* this use of intensity images can be misleading and miss grains of similar orientations that are adjacent to each other such as grains 1 and 2 in *Figure 3*. Due to the shortcoming of using intensity maps as an indication of microstructure, correlative microscopy should be performed if statements about grain structure and stresses are to be made.

The calculated  $\sigma_m$  maps from the PLS data with 0, 100, and 150 MPa of applied uniaxial stress, which corresponds to  $\sigma_m$  values of 0, 33, and 50 MPa, are displayed in Figure 4. From first observations, the contour maps show a large spatial distribution of stresses due to the anisotropy of corundum alumina as reported previously[12, 13]. With an applied tensile stress, the regions of high tensile stress (red) begin to grow and the areas of high compressive stress (blue) begin to shrink, as would be expected. The average of each calculated  $\sigma_m$  measurement in Figure 4 was calculated and reported in Table 2, along with its standard deviation/distribution. The average stress of the microstructure is within 5 MPa of the applied stress when accounting for the initial compressive stress in the microstructure, showing the validity of the technique. The stress distributions (Figure 5) for the microstructure have a normal fit and the shape of this distribution does not change with an applied stress. Only that the normal stress distribution shifts towards tension with an applied tensile load. This suggests that there is no stress redistribution with an applied load, but only that the applied stress directly applies to the residuals stresses that are intrinsically within the microstructure.

The average stresses within the microstructure are relatively quite low and increase with applied load, while the max tensile stresses are an order of magnitude higher (Table 2), than the average applied  $\sigma_m$ . It is the intersection of these high stress regions with a critical flaw where the material failure will initiate(Table 2)[4]. Understanding only the mean stress does little to inform failure predictions of a brittle material. This illustrates the importance of understanding the full stress state within brittle material microstructures for modeling to become truly predictive. The ability of PLS to provide first of a kind data to help improve these models is groundbreaking, and will enable the improvement of microstructure level models in brittle materials.

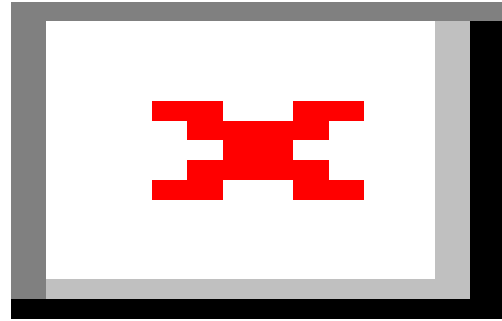


Figure 3: Inverse pole figure (a) and R1 intensity map (b), showing the inability of intensity maps to detect adjacent grains with similar orientations (grain 1 and 2).

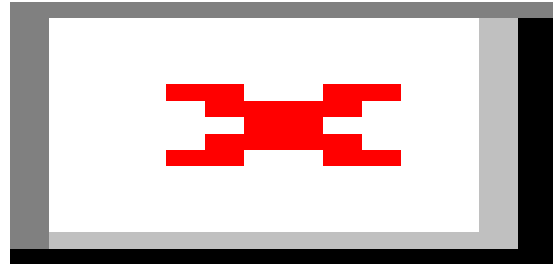


Figure 4:  $\sigma_m$  PLS maps of region with a) zero applied  $\sigma_m$  b) 33.3 MPa applied  $\sigma_m$  c) 50 MPa applied  $\sigma_m$

Table 2: Measured stresses as function of applied load.

Applied $\sigma_m$	0 MPa	33.3 MPa	50 MPa
Average $\sigma_m$ (MPa)	-9.1	22.5	36.8
Standard Dev.	43.2	41.4	42.2
Min $\sigma_m$ (MPa)	-154.9	-128.0	-114.9
Max $\sigma_m$ (MPa)	191.2	204.6	216.9

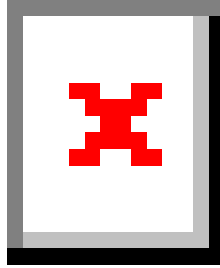


Figure 5: Stress distribution of three loading conditions.

## 4.2. Modeling

The 2D plane stress  $\sigma_m$  maps obtained using MOOSE are seen in *Figure 6*. The mean, max and minimum stresses are given in *Table 3*. As expected the compressive stresses decrease, while the max tensile stress increases with increasing load. In comparing the simulated and experimental results, there is general agreement observed with areas of compression and tension. However, the peak stresses predicted in the simulation are a factor of two higher than those measured using PLS. This discrepancy is likely due to four main factors: stress singularities at the highly-resolved grain boundaries in the model, the lower resolution of the measurement at the grain boundaries due to the  $\sim 2 \mu\text{m}^3$  interaction volume, the assumption in the model that the grains are perfectly bonded, and the 2D plane stress assumption.

The mesh used in the models is highly refined at the grain boundaries to resolve them accurately in space; however, this provides less averaging of stresses compared to the experimental measurement. The element size near grain boundaries is on the order of a  $0.1\mu\text{m}$  vs the  $0.87\mu\text{m}$  spot size used in the mapping measurements. Therefore, the model resolves the higher stresses at/near grain boundaries while the measurement averages over a larger area further from the peak stresses which occur at the boundaries. To enable a better comparison the simulated results were averaged along a 1 micron rectangular grid to better align with the measurement size (*Table 3*).

Averaging the simulation results over the 1 micron area resulted in reduction of the peak observed stresses by  $\sim 30\%$ , bringing them closer the measured peak stress values. The observed higher peak stresses at the grain boundaries in the model are also partially due to the assumption of perfect bonding between grains. This is a simplifying assumption for the model; although, in practice micro-cracking and composition differences at grain boundaries are observed in alumina resulting in imperfect bonding[22-25]. Unfortunately, there is no agreed upon value for the strength of the bonding between grains in alumina [23]. Future work could include varying the bonding between grains to more closely match measured stresses.

The larger interaction volume, particularly in the z-direction (depth), is also the cause of the poorer agreement between areas of small grains vs larger grains in the microstructure. Due to the 2-3 micron depth at which PLS signal is generated there is higher probability of sampling another subsurface grain in an area of small grains, whereas in large grains it is more likely that the signal is coming entirely within the grain on the surface. Additionally, if several grains exist in the measured volume the assumption of plane stress becomes less accurate of sample behavior.

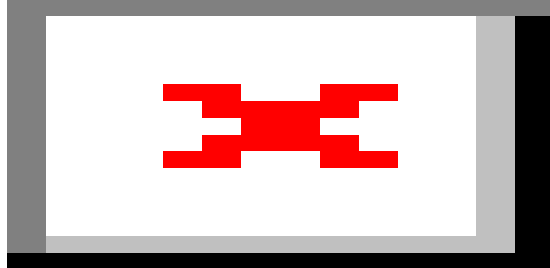


*Figure 6: Simulated  $\sigma_m$  maps for three loading conditions a) zero applied  $\sigma_m$  b) 33.3 MPa applied  $\sigma_m$  c) 50 MPa applied  $\sigma_m$*

Table 3: Calculated stresses as function of applied load and averaging area.

5. Applied $\sigma_m$	0 MPa no averaging	0 MPa 1 $\mu\text{m}$	33.3 MPa no averaging	33.3 MPa 1 $\mu\text{m}$	50 MPa no averaging	50 MPa 1 $\mu\text{m}$
<b>Average <math>\sigma_m</math> (MPa)</b>	0	0	33.7	33.4	50.1	50.2
<b>Min <math>\sigma_m</math> (MPa)</b>	-244.5	-227.7	-208.1	-194.6	-192.4	-166.4
<b>Max <math>\sigma_m</math> (MPa)</b>	377.2	250.4	399.8	282.5	411.1	298.6

## ONCLUSIONS

PLS was successfully used to investigate the residual and applied stresses in polycrystalline alumina. PLS was able to accurately resolve stresses at the microstructure level with a spatial resolution of 2 microns. The average measured stresses matched to known applied loads within one standard deviation, showing the accuracy of this high spatially resolved technique for the first time. Measurements found that max local stresses within the microstructure were an order of magnitude higher than that of the average stress. These high local stresses are the likely areas of failure, and understanding their location and occurrence are critical to enabling the prediction of failure in brittle materials. The modeling efforts produced general agreement of the spatial location of max compressive and tensile stresses to the experimental results using simplifying assumptions such as 2D microstructure and perfect bonding between grains. However, further refinement of the models to incorporate additional mechanisms such as micro-cracking, grain boundary complexions, and 3D microstructure is required to achieve higher fidelity results. Microstructure scale modeling is primed to take advantage of PLS to enable its refinement and validation, eventually enabling microstructure modeling to become a predictive tool for brittle materials.

## Acknowledgements

Sandia National Laboratories is a multimission laboratory managed and operated by National Technology and Engineering Solutions of Sandia LLC, a wholly owned subsidiary of Honeywell International Inc. for the U.S. Department of Energy's National Nuclear Security Administration under contract DE-NA0003525.



## REFERENCES

1. Ritter, J.E., *Engineering design and fatigue failure of brittle materials*. Crack Growth and Microstructure, 1978: p. 667-686.
2. Farag, M.M., *Materials and process selection for engineering design*. 2013: CRC Press.
3. Rödel, J., et al., *Development of a roadmap for advanced ceramics: 2010–2025*. Journal of the European Ceramic Society, 2009. **29**(9): p. 1549-1560.
4. Wachtman, J.B., W.R. Cannon, and M.J. Matthewson, *Mechanical properties of ceramics*. 2009: John Wiley & Sons.
5. Takano, N., et al., *Microstructure-based stress analysis and evaluation for porous ceramics by homogenization method with digital image-based modeling*. International Journal of Solids and Structures, 2003. **40**(5): p. 1225-1242.
6. Alexander, K.B., et al., *Internal Stresses and the Martensite Start Temperature in Alumina-Zirconia Composites: Effects of Composition and Microstructure*. Journal of the American Ceramic Society, 1995. **78**(2): p. 291-296.
7. Messaoudi, K., A. Huntz, and L. Di Menza, *Residual stresses in alumina scales. Experiments, modeling, and stress-relaxation phenomena*. Oxidation of metals, 2000. **53**(1-2): p. 49-75.
8. Vedula, V.R., et al., *Residual-Stress Predictions in Polycrystalline Alumina*. Journal of the American Ceramic Society, 2001. **84**(12): p. 2947-2954.
9. Keleş, Ö., R.E. García, and K.J. Bowman, *Stochastic failure of isotropic, brittle materials with uniform porosity*. Acta Materialia, 2013. **61**(8): p. 2853-2862.
10. Reid, A.C., et al., *Modelling microstructures with OOF2*. International Journal of Materials and Product Technology, 2009. **35**(3-4): p. 361-373.
11. Watts, J., et al., *Measurement of thermal residual stresses in ZrB<sub>2</sub>–SiC composites*. Journal of the European Ceramic Society, 2011. **31**(9): p. 1811-1820.
12. Michaels, C.A. and R.F. Cook, *Determination of residual stress distributions in polycrystalline alumina using fluorescence microscopy*. Materials & Design, 2016. **107**: p. 478-490.
13. Myers, G.A., C.A. Michaels, and R.F. Cook, *Quantitative mapping of stress heterogeneity in polycrystalline alumina using hyperspectral fluorescence microscopy*. Acta Materialia, 2016. **106**: p. 272-282.
14. Cook, R.F., et al., *Sigmoidal Indentation–Strength Characteristics of Polycrystalline Alumina*. Journal of the American Ceramic Society, 1994. **77**(2): p. 303-314.
15. Munro, R.G., et al., *Model line-shape analysis for the ruby R lines used for pressure measurement*. Journal of Applied Physics, 1985. **57**(2): p. 165-169.
16. Lipkin, D.a. and D. Clarke, *Measurement of the stress in oxide scales formed by oxidation of alumina-forming alloys*. Oxidation of Metals, 1996. **45**(3): p. 267-280.
17. Christensen, R., et al., *Nondestructive evaluation of the oxidation stresses through thermal barrier coatings using Cr<sup>3+</sup> piezospectroscopy*. Applied Physics Letters, 1996. **69**(24): p. 3754-3756.
18. Langer, S.A., E.R. Fuller Jr, and W.C. Carter, *OOF: image-based finite-element analysis of material microstructures*. Computing in Science & Engineering, 2001. **3**(3): p. 15-23.
19. Gaston, D., et al., *MOOSE: A parallel computational framework for coupled systems of nonlinear equations*. Nuclear Engineering and Design, 2009. **239**(10): p. 1768-1778.

20. Goto, T., et al., *Elastic constants of corundum up to 1825 K*. Journal of Geophysical Research: Solid Earth, 1989. **94**(B6): p. 7588-7602.
21. Wachtman, J.B., T.G. Scuderi, and G.W. Cleek, *Linear Thermal Expansion of Aluminum Oxide and Thorium Oxide from 100° to 1100°K*. Journal of the American Ceramic Society, 1962. **45**(7): p. 319-323.
22. Evans, A. and K. Faber, *Crack-growth resistance of microcracking brittle materials*. Journal of the American ceramic society, 1984. **67**(4): p. 255-260.
23. Buban, J., et al., *Grain boundary strengthening in alumina by rare earth impurities*. Science, 2006. **311**(5758): p. 212-215.
24. Swanson, P.L., et al., *Crack-Interface Grain Bridging as a Fracture Resistance I, Mechanism in Ceramics: I, Experimental Study on Alumina*. Journal of the American Ceramic Society, 1987. **70**(4): p. 279-289.
25. Kružic, J., R. Cannon, and R. Ritchie, *Effects of Moisture on Grain-Boundary Strength, Fracture, and Fatigue Properties of Alumina*. Journal of the American Ceramic Society, 2005. **88**(8): p. 2236-2245.



## **DISTRIBUTION**

1	MS0346	Scott Grutzik	1556
1	MS0549	Melissa Teague	5876
1	MS0889	Hartono Sumali	1851
1	MS1411	Theron Rodgers	1814
1	MS1411	Stephen Meserole	1816
1	MS0899	Technical Library	9536 (electronic copy)
1	MS0359	D. Chavez, LDRD Office	1911



**Sandia National Laboratories**